Ye et al. *Zool. Res.* 2024, 45(5): 1073−1087
https://doi.org/10.24272/j.issn.2095-8137.2024.019
https://cstr.cn/32248.14.zr.2024.019

ZR | Zoological Research

Article Open Access

Homozygous *CCDC146* mutation causes oligoasthenoteratozoospermia in humans and mice

Jing-Wei Ye[1,#], Tanveer Abbas[1,#], Jian-Teng Zhou[1], Jing Chen[1], Meng-Lei Yang[1], Xiong-Heng Huang[1], Huan Zhang[1], Hui Ma[1], Ao Ma[1,2], Bo Xu[1], Ghulam Murtaza[1], Qing-Hua Shi[1,*], Bao-Lu Shi[1,*]

[1] *Division of Reproduction and Genetics*, *First Affiliated Hospital of University of Science and Technology of China*, *Hefei National Laboratory for Physical Sciences at Microscale*, *School of Basic Medical Sciences*, *Division of Life Sciences and Medicine*, *Biomedical Sciences and Health Laboratory of Anhui Province*, *Institute of Health and Medicine*, *Hefei Comprehensive National Science Center*, *University of Science and Technology of China*, *Hefei*, *Anhui* 230026, *China*

[2] *Institute of Andrology*, *Nanjing Drum Tower Hospital*, *Affiliated Hospital of Nanjing University Medical School*, *Nanjing*, *Jiangsu* 210008, *China*

ABSTRACT

Infertility represents a significant health concern, with sperm quantity and quality being crucial determinants of male fertility. Oligoasthenoteratozoospermia (OAT) is characterized by reduced sperm motility, lower sperm concentration, and morphological abnormalities in sperm heads and flagella. Although variants in several genes have been implicated in OAT, its genetic etiologies and pathogenetic mechanisms remain inadequately understood. In this study, we identified a homozygous nonsense mutation (c.916C>T, p.Arg306*) in the coiled-coil domain containing 146 (*CCDC146*) gene in an infertile male patient with OAT. This mutation resulted in the production of a truncated CCDC146 protein (amino acids 1–305), retaining only two out of five coiled-coil domains. To validate the pathogenicity of the *CCDC146* mutation, we generated a mouse model (*Ccdc146*$^{mut/mut}$) with a similar mutation to that of the patient. Consistently, the *Ccdc146*$^{mut/mut}$ mice exhibited infertility, characterized by significantly reduced sperm counts, diminished motility, and multiple defects in sperm heads and flagella. Furthermore, the levels of axonemal proteins, including DNAH17, DNAH1, and SPAG6, were significantly reduced in the sperm of *Ccdc146*$^{mut/mut}$ mice. Additionally, both human and mouse CCDC146 interacted with intraflagellar transport protein 20 (IFT20), but this interaction was lost in the mutated versions, leading to the degradation of IFT20. This study identified a novel deleterious homozygous nonsense mutation in *CCDC146* that causes male infertility, potentially by disrupting axonemal protein transportation. These findings offer valuable insights for genetic counseling and understanding the mechanisms underlying *CCDC146* mutant-associated infertility in human males.

Keywords: Oligoasthenoteratozoospermia; Human infertility; Sperm flagellum; CCDC146; Intraflagellar transport; IFT20

INTRODUCTION

Infertility is a major health concern, affecting approximately 17.5% of the global population (Njagi et al., 2023), with male infertility being the primary factor in half of infertile couples (Agarwal et al., 2021). Key determinants of male fertility include sperm quantity, vitality, motility, morphology, and fertilizing capacity, with defects in any potentially causing male infertility (Sang et al., 2023). The World Health Organization (WHO) (2021) defines oligoasthenoteratozoospermia (OAT) as having less than 30% progressively motile sperm, a sperm concentration below 16 million/mL, and fewer than 4% morphologically normal sperm. Multiple morphological abnormalities of the sperm flagella (MMAF), a specific subtype of OAT, is characterized by various deformities including short, coiled, absent, or irregular flagella (Chang et al., 2023).

Sperm flagella are specialized, evolutionarily conserved organelles critical for sperm motility. The core axoneme structure of each flagellum consists of nine peripheral

Received: 11 May 2024; Accepted: 11 June 2024; Online: 12 June 2024

Foundation items: This work was supported by the National Key Research and Developmental Program of China (2021YFC2700202, 2022YFC2702601, 2019YFA0802600, 2022YFA0806303), National Natural Science Foundation of China (32470915, 32000587, 32270901, 82171601), Global Select Project (DJK-LX-2022010) of the Institute of Health and Medicine, Hefei Comprehensive National Science Center, Joint Fund for New Medicine of USTC (YD9100002034), and Scientific Research Foundation for Scholars of the First Affiliated Hospital of USTC (RC2023054)

[#]Authors contributed equally to this work

*Corresponding authors, E-mail: qshi@ustc.edu.cn; bl625@ustc.edu.cn

microtubule doublets (MTDs) and a central pair of microtubule singlets (CP), along with numerous axonemal proteins (Touré et al., 2021). These proteins assemble into several functional components, providing the necessary force for flagellar beating and maintaining the structural integrity of the sperm flagella. Inadequate expression or mislocalization of these proteins, often due to mutations in their corresponding genes, has been frequently observed in individuals with MMAF or OAT (Sang et al., 2023; Touré et al., 2021; Wang et al., 2022b). However, approximately 40% of MMAF or OAT cases are linked to unknown factors, reflecting the complex genetic background of humans (Lu et al., 2021). This highlights the necessity for a more precise and comprehensive understanding of the genetic factors contributing to OAT-related male infertility.

Due to the absence of ribosomes in cilia and flagella, the translation of various axonemal proteins occurs in the cytoplasm of cell bodies. Efficient import and precise delivery of axonemal proteins are facilitated by the intraflagellar transport (IFT) system (Finetti et al., 2022; Pazour et al., 2005). This system is composed of 22 proteins, which interact with cytoplasmic dynein and kinesin and are categorized into two complexes, IFT-A and IFT-B, responsible for retrograde and anterograde transport, respectively (Lacey et al., 2023). Variations in the genes encoding IFT proteins typically result in severe ciliopathies, reflecting deficiencies in cilium development in humans (Fassad et al., 2023; Pazour & Rosenbaum, 2002; Schmidts et al., 2013; Shaheen et al., 2020; Taschner & Lorentzen, 2016). The pivotal roles of IFT proteins in spermiogenesis have been substantiated through genetically modified mouse models (Liu et al., 2017; San Agustin et al., 2015; Zhang et al., 2016, 2017, 2018). Several axonemal proteins are also believed to participate in IFT processes, facilitating the growth of sperm flagella. Deletion of these axonemal proteins often leads to impaired expression or localization of IFT components and cargos (Cong et al., 2022; Tian et al., 2023; Wu et al., 2021; Zhang et al., 2022). However, there is currently insufficient or unreliable evidence to support the direct involvement of these flagellar proteins in the assembly or maintenance of IFT trains.

Coiled-coil domains, characterized by alpha-helical peptides that coil around each other, are present in a wide range of proteins (Priyanka & Yenugu, 2021). Proteins within the coiled-coil domain containing (CCDC) family are integral to male reproduction, playing key roles in chromosome movement, centriole architecture, axoneme assembly, and flagellar beating (Chen et al., 2021; Liu et al., 2023; Sha et al., 2020; Yang et al., 2022). The coiled-coil domain containing 146 (CCDC146) protein, initially identified in bovine sperm centrosomes (Firat-Karalar et al., 2014), has recently been recognized for its crucial roles in mouse spermiogenesis. Notably, it facilitates the transportation of outer dense fibers (ODFs) in conjunction with CCDC38 and CCDC42 (Ma et al., 2024) and probably functions as a microtubule-associated protein, co-localizing with tubulin in sperm flagella (Muroňová et al., 2024). Mutations in the *CCDC146* gene have also been identified in infertile men with MMAF (Muroňová et al., 2024); however, the pathogenic mechanisms leading to spermiogenesis failure due to *CCDC146* mutations remain to be elucidated.

In this study, we enrolled an infertile patient, born to first-cousin parents, who exhibited severe OAT. Using whole-exome sequencing (WES) and Sanger sequencing, we identified a novel homozygous nonsense mutation (c.916C>T, p.Arg306*) in the *CCDC146* gene, which co-segregated with OAT within the family. To validate the pathogenicity of this mutation, we generated *Ccdc146* mutant mice (*Ccdc146*$^{mut/mut}$) harboring the same mutation. Notably, these mutant mice also exhibited OAT, corroborating the deleterious impact of the *CCDC146* mutation on male fertility in both humans and mice. Further studies revealed that CCDC146 was essential for the transportation of axonemal proteins into sperm flagella, potentially mediated by the interaction between intraflagellar transport protein 20 (IFT20) and the C-terminus of the CCDC146 protein, a region deleted in both the patient and *Ccdc146*$^{mut/mut}$ mice. These findings indicate that CCDC146 plays a conserved role in intraflagellar transport in both species, and the c.916C>T mutation is a causative factor for OAT.

MATERIALS AND METHODS

Participants

This study was approved by the Institutional Ethics Committee of University of Science and Technology of China (USTC) (approval number: 2019-KY-168). A consanguineous Pakistani family, including an infertile male, was recruited in this study. Written informed consent was obtained from all participants prior to the commencement of the study. Semen parameters, including semen volume, sperm concentration, and sperm motility, were evaluated twice for the patient according to the WHO guidelines (World Health Organization, 2021). Ultrasonography of the patient's scrotum was performed using an 11 MHz probe at local laboratories. Primary ciliary dyskinesia (PCD)-associated symptoms, such as chronic respiratory distress, were excluded during medical consultation. Samples from fertile controls were obtained from volunteers at the First Affiliated Hospital of USTC.

WES and variant filtration

Total genomic DNA was isolated from the peripheral blood of individuals III:1, III:2, and IV:2 using a FlexiGene DNA Kit (QIAGEN, Germany) and fragmented using a Covaris focused-ultrasonicator (USA). Whole-exome capture and sequencing were performed using an AIExome Enrichment Kit V1 (iGeneTech, China) and the Hiseq2000 platform (Illumina, USA) following standard procedures. Reads were aligned to the human genome reference assembly (hg19) using BWA-MEM with default parameters (Li, 2013), and polymerase chain reaction (PCR) duplicates were removed using Picard software (http://broadinstitute.github.io/picard/). DNA sequence variants were called using the Genome Analysis Toolkit HaplotypeCaller (http://www.broadinstitute.org/gatk/). Variants were annotated using ANNOVAR (Wang et al., 2010), and candidate pathogenic variant filtration was conducted as described previously (Fan et al., 2021; Gong et al., 2022; Ma et al., 2023; Shi et al., 2023; Yin et al., 2019; Zhang et al., 2020). Details are provided in Supplementary Figure S1 and Tables S1, S2. Runs of homozygosity were detected using Bcftools (Narasimhan et al., 2016), with runs over 1.5 Mb used to calculate inbreeding coefficients with an in-house script. Family member relatedness was verified using Peddy (Pedersen & Quinlan, 2017). Primer sequences for Sanger sequencing are listed in Supplementary Table S3.

Electron microscopy

Fresh semen samples from the patient were centrifuged at 1 000 ×*g* for 3 min at room temperature. Mouse spermatozoa collected from the cauda epididymis were centrifuged at 1 000 ×*g* for 3 min at room temperature. The spermatozoa were washed with phosphate-buffered saline (PBS) three times, then fixed in 0.1 mol/L phosphate buffer (pH 7.4) containing 4% glutaraldehyde, 4% paraformaldehyde (PFA), and 0.2% picric acid at 4°C for at least 12 h. Scanning and transmission electron microscopy analyses were performed as described previously (Ma et al., 2021, 2022a).

Hematoxylin and eosin (H&E) staining

Human semen smears were prepared following WHO guidelines, with at least 200 spermatozoa per individual analyzed for morphology, recording the heads, necks, and tails separately. Mouse sperm smears were prepared using sperm released from the cauda epididymis. The smears were fixed in 4% PFA at room temperature for 5 min, washed three times in PBS, then stained with hematoxylin for 30 min and eosin for 10 min. For each mouse, at least 200 spermatozoa were analyzed for morphological features. Mouse tissue sections (testis, epididymis, lung, and trachea) were processed as per previous research (Ma et al., 2023). Images were captured using an Olympus BX53 microscope with an SC180 camera and cellSens Dimension v.3.1.1 software (Japan).

Generation of *Ccdc146* mutant (*Ccdc146*$^{mut/mut}$) mice

Ccdc146$^{mut/mut}$ mice were generated using CRISPR/Cas9 technology as per our previous studies (Liu et al., 2022; Ma et al., 2023), with minor modifications. Briefly, a guide RNA (gRNA) was designed near the mutation site in exon 8 and was transcribed *in vitro* (ThermoFisher Scientific AM1908, USA). A single-strand oligodeoxynucleotide 130 nucleotides (nt) long containing the desired base changes at the mutation site was synthesized and electroporated into C57BL/6 mouse zygotes along with the gRNA and Cas9 protein (Integrated DNA Technologies 1081058, USA). The zygotes were then transferred into the oviduct ampullae of pseudo-pregnant ICR females. Pup genotypes were determined through PCR amplification of genomic DNA from finger biopsies and subsequent Sanger sequencing. The gRNA sequence was 5′-GAAGTCAAAGAACGAGAGTA-3 ′, and the genotyping primers are listed in Supplementary Table S3. The C57BL/6 and ICR mice were purchased from Beijing Vital River Laboratory Animal Technology Co. Ltd. (China). All animal experiments were approved by the Institutional Animal Care and Use Committee of USTC (approval number: USTCACUC1301021) and conducted in accordance with their guidelines.

Fertility test and sperm parameters

Eight-week-old homozygous mutant mice from at least the F2 generation were used for phenotypic analysis. Each male was mated with two females over a period of three months to assess fertility. Testes and epididymides were dissected immediately after cervical dislocation. Sperm counts were determined using hemocytometers under a microscope after the sperm were released into PBS by cutting and incubating the epididymis at 37°C for 30 min. Sperm motility was analyzed using computer-aided sperm analysis (CASA) as described previously (Liu et al., 2022; Ma et al., 2023). Sperm morphology was assessed following smear slide preparation and H&E staining.

RNA extraction and reverse-transcription PCR (RT-PCR)

Total RNA was extracted from human peripheral blood and mouse tissue, with subsequent synthesis of cDNA performed following previous study (Gong et al., 2022). For cDNA obtained from peripheral blood, PCR conditions were: 5 min at 94°C, followed by 36 cycles of 30 s at 94°C, 30 s at 60°C, and 20 s at 72°C. For cDNA obtained from mouse tissues, PCR reactions were: 5 min at 94°C, followed by 34 cycles of 30 s at 94°C, 30 s at 60°C, and 15 s at 72°C. Primer sequences are listed in Supplementary Table S3.

Western blotting

Testicular tissues from adult mice were lysed in lysis buffer (50 mmol/L Tris, 150 mmol/L NaCl, 0.5% Triton X-100, and 5 mmol/L ethylenediaminetetraacetic acid (EDTA), pH 7.5) containing a protease inhibitor cocktail (PIC) (Solarbio P6730, China) and phenylmethylsulfonyl fluoride (PMSF) (Solarbio P8340, China), then homogenized in Dounce tissue grinders and subjected to sonication. Epididymal spermatozoa from mice were centrifuged at 1 000 ×*g* for 3 min at room temperature to remove the supernatant before lysis and sonication. Cultured cells were lysed directly in lysis buffer after medium removal. Western blot analysis was performed as described previously (Ma et al., 2022b). Details of the primary and secondary antibodies are listed in Supplementary Table S4. Original western blot images are presented in Supplementary Figure S2.

Plasmid construction and cell transfection

Full-length coding sequences of human *CCDC146* and *IFT20* were amplified from testicular tissues of obstructive azoospermia (OA) patients through total RNA extraction and reverse transcription. Full-length coding sequences of mouse *Ccdc146* and *Ift20* were amplified from testicular tissues of adult wild-type (WT) mice. The full-length coding sequence of mouse *Ccdc146* with the nonsense mutation was directly amplified from testicular tissues of adult *Ccdc146*$^{mut/mut}$ mice. These DNA fragments were then fused to the C terminus of human influenza hemagglutinin (HA) tags or green fluorescent protein (GFP) on pN1 vectors. Plasmids expressing mutant (MT) human CCDC146 protein were generated through site-directed mutagenesis of the human CCDC146 full-length protein-expressing plasmid using two pairs of primers (humanCCDC146-MT-F and HA-humanCCDC146-FL-R, pN1-HA-F and humanCCDC146-MT-R). A plasmid encoding the mouse IFT88 protein with GFP fused to the C terminus (mIFT88-GFP) was constructed in previous research (Ma et al., 2024). Primer sequences are listed in Supplementary Table S3.

HEK293T cells were cultured in 6-well or 24-well plates in Dulbecco's modified Eagle medium (DMEM) supplemented with 10% fetal bovine serum (FBS) under standard conditions (37°C, 5% CO_2). The cells were transfected with the indicated plasmids using Lipofectamine 3000 reagents (ThermoFisher Scientific L3000015, USA) according to the manufacturer's instructions.

Co-immunoprecipitation (co-IP)

HEK293T cells were washed in PBS after 36 h of transfection and lysed in lysis buffer with PIC and PMSF on a shaker at 4°C for 20 min. The cell lysates were incubated with anti-GFP nanobody magnetic beads (AlpalifeBio KTSM1334, Shenzhen, China) at 4°C overnight, washed in lysis buffer four times, and

denatured for 10 min before western blot analysis.

Testicular cell smear preparation

After removal of the tunica albuginea, mouse testicular tissues were minced into small pieces in PBS and filtered through a 100-mesh cell strainer. A 20 μL cell suspension was mixed with 60 μL of 4% PFA on each glass slide, and a coverslip was applied to spread the cells. The slides were air-dried at room temperature, immersed in PBS containing 0.2% Triton X-100 (PBST) and 4% PFA for 10 min to remove the coverslips, and washed three times in PBST. The slides were then subjected to antigen retrieval in hot citrate buffer for 10 min, followed by permeabilization in PBST for 15 min, with subsequent processes described in the immunofluorescence staining section.

Testicular cell squash preparation

Testicular cell squashes were prepared as described in previous research (Wellard et al., 2018), with minor modifications. Briefly, after removing the tunica albuginea, mouse seminiferous tubules were isolated and fixed in freshly prepared PBS containing 1% PFA and 0.1% Triton X-100 (pH 9.0) at room temperature for 5–10 min. The tubules were then cut into 2–3 mm segments, with 10–20 segments transferred onto a glass slide containing a small amount of fixative. The segments were arranged to avoid overlap, and coverslips were applied to disperse the testicular cells. The slides were frozen in liquid nitrogen for 15 s, the coverslips were removed, and the slides were washed in PBS for 10 min and in PBST for 10 s. The slides were then processed according to the immunofluorescence staining protocols.

Immunofluorescence staining

Immunofluorescence staining of mouse testicular sections, testicular cell smears, and sperm smears was performed following previously described protocols (Xu et al., 2022; Ma et al., 2023). Fluorescent images were captured using an Olympus BX53 microscope with a Photometrics Prime BSI camera and cellSens Dimension software v.3.1.1 (Tokyo, Japan). Primary and secondary antibodies used are listed in Supplementary Table S4.

Statistical analysis

Statistical analyses were performed using GraphPad Prism v.8.0 (GraphPad Software, USA). Values in tables and graphs are presented as mean±standard error of the mean (SEM). Comparisons between two groups were conducted using Student's *t*-test for independent samples. Differences were considered significant at $P<0.05$.

RESULTS

Clinical characteristics of an infertile male diagnosed with OAT

To identify novel mutations causing male infertility, we recruited a Pakistani family with a man suffering from idiopathic infertility, born to first-cousin parents (Figure 1A; Table 1). Despite normal physiological development, the patient had been unable to conceive after 11 years of marriage (Table 1). Cytogenetic analysis revealed a normal karyotype with no Y-chromosome microdeletions. Scrotal ultrasonography showed normal morphology of the testes and epididymides (Table 1; Supplementary Figure S3). Semen analyses, conducted twice according to WHO guidelines, consistently demonstrated a significantly reduced sperm count and impaired motility, particularly progressive motility, while semen volume and pH remained within normal ranges. These findings suggested that the patient exhibited typical characteristics associated with oligoasthenozoospermia (Table 1).

To assess sperm morphology, smear slides were prepared and subjected to H&E staining. Various defects were identified: 75.14% of sperm displayed head abnormalities, such as tapered or amorphous head shapes; 60.09% exhibited neck defects, including bent or asymmetrical necks; and 72.65% displayed flagellar abnormalities, including absent, short, double, or irregular-caliber flagella (Table 1; Supplementary Figure S4). Scanning electron microscopy further validated these findings, revealing no normal sperm morphology, with most displaying absent, short, or irregular flagella and deformed heads (Figure 1B). Subtle structural defects in the head and neck regions, which may appear normal under light microscopy, were also observed (Figure 1B). Transmission electron microscopy was then utilized to examine the axonemal and peri-axonemal structures within the flagella. Aberrations included the absence of peripheral microtubule doublets or central microtubule singlets, disorganized microtubules, abnormally distributed longitudinal columns or fibrous sheaths (Figure 1C). These findings indicated that the sperm from our patient with oligoasthenozoospermia exhibited defects in both the heads and flagella, confirming a diagnosis of OAT.

Identification of a homozygous nonsense mutation in *CCDC146*

To identify potential pathogenic mutations, WES and bioinformatic analysis were performed on the patient and his parents. After extensive screening, a homozygous nonsense mutation (c.916C>T, p.Arg306*) in *CCDC146* (NM_020879.3) was identified (Supplementary Figure S1 and Table S1). This mutation, which occurs at very low frequencies in human genomic variation databases (Supplementary Table S2), co-segregated with male infertility in this family, as evidenced by Sanger sequencing (Figure 1A). According to the Human Protein Atlas, *CCDC146* is highly expressed in the human testis and oviduct, with mRNA enrichment in spermatocytes and early spermatids during spermatogenesis (Supplementary Figure S5A, B). Furthermore, CCDC146 proteins in humans and mice exhibit a high degree of conservation, sharing approximately 76% identity in their amino acid sequences and similar expression profiles (Supplementary Figure S5C–E). Mice lacking CCDC146 demonstrate impaired sperm morphology and motility, resulting in male infertility (Ma et al., 2024; Muroňová et al., 2024), implying an essential role of CCDC146 in human spermiogenesis.

The identified nonsense mutation in *CCDC146* caused the premature termination of protein translation at amino acid position 306, resulting in the production of a truncated protein (Figure 1D). This truncation resulted in the loss of about 68% of the CCDC146 protein from the C terminus, including three out of five coiled-coil domains probably crucial for interactions between CCDC146 and other proteins (Figure 1D). Furthermore, while CCDC146 is localized along the entire axoneme of normal human sperm, its signal was absent in the patient's sperm due to the loss of antibody epitopes at the C terminus (amino acids 826–955) (Figure 1E). To ascertain whether the *CCDC146* mutation resulted in a truncated protein, RT-PCR was first performed to evaluate the

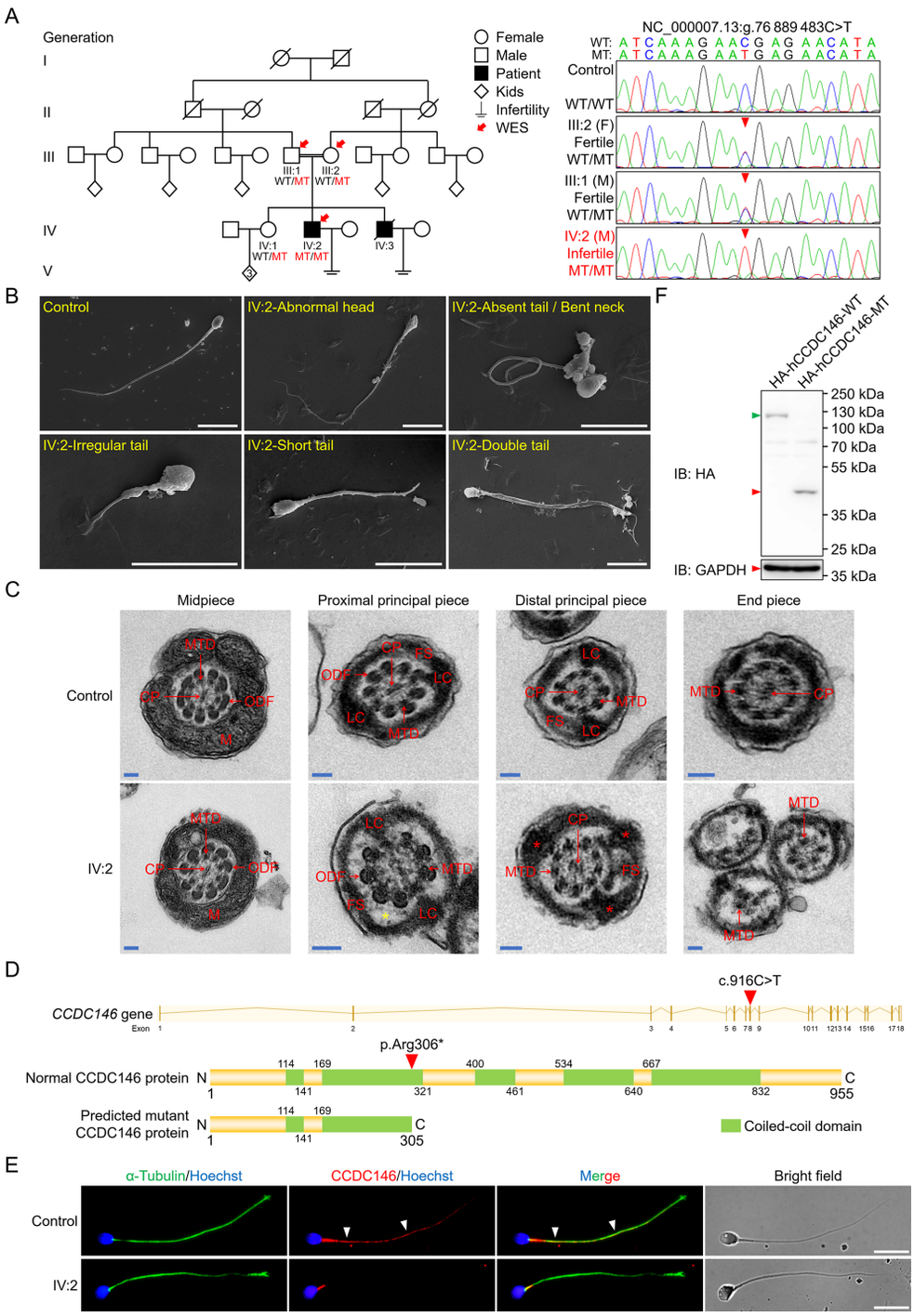

Figure 1 Homozygous *CCDC146* nonsense mutation identified in an infertile man with abnormal sperm morphology

A: Pedigree of consanguineous family with one infertile patient (IV:2). Arrows point to individuals for whom WES was performed. Slashes stand for deceased family members, and double horizontal lines represent consanguineous union. Sanger sequencing validation of *CCDC146* nonsense mutation (NC_000007.13:g.76 889 483C>T) in available family members and fertile control is shown on the right with mutant bases indicated by red arrowheads. F, female; M, male; WT, wild-type allele; MT, mutant allele. B: Representative scanning electron micrographs displaying typical abnormalities of sperm heads, necks, or tails observed in IV:2. Representative normal spermatozoon from fertile control is shown. Scale bars: 10 μm. C: Representative transmission electron micrographs of sperm flagellar cross-sections from fertile control and IV:2. Scale bars: 100 nm. M, mitochondria; MTD, microtubule doublets; CP, central pair; ODF, outer dense fiber; LC, longitudinal column; FS, fibrous sheath. Red asterisks indicate abnormally distributed LCs in principal piece. Yellow asterisk indicates extra space between MTD and FS. D: Position of nonsense mutation in exon 8 of human *CCDC146* (NCBI reference sequence No. NM_020879.3) (https://www.ncbi.nlm.nih.gov/nuccore/NM_020879.3/) and within second coiled-coil domain of CCDC146 protein (UniProt accession No. Q8IYE0) (https://www.uniprot.org/uniprotkb/Q8IYE0/entry/). Predicted CCDC146 truncated protein is shown. E: Representative images of sperm stained with anti-CCDC146-C antibody from IV:2 and fertile control. Anti-α-tubulin antibody was used to label microtubules. Arrowheads indicate specific signals along flagella of control sperm. Scale bars: 10 μm. F: Immunoblotting of HEK293T cells with anti-HA antibody after 24 h of expression of HA-tagged human CCDC146 proteins. Green and red arrowheads indicate normal and mutant proteins, respectively. GAPDH was used as the loading control.

Table 1 Clinical characteristics of infertile male

	Fertile control	IV:2	Reference values
Genotype for *CCDC146*	–	MT/MT	–
Age (years)	–	30	–
Height/Weight (cm/kg)	–	167/74	–
Years of marriage	–	11	–
Ultrasonography[1]			
Testis size (cm×cm)	ND	Left: 3.3×1.6 Right: 3.5×1.7	4×2.5
Epididymis size (cm×cm)	ND	Left: 1.4×0.6 Right: 1.1×0.7	1.2×0.6
Semen parameters[2]			
Semen volume	ND	2.83±0.28	>1.4
Semen pH	ND	Alkaline	Alkaline
Sperm concentration (10^6/mL)	ND	5.13±0.71	>16.0
Motile sperm (%)	ND	19.56±6.07	>42.0
Progressively motile sperm (%)	ND	8.89±3.63	>30.0
Sperm morphology[2]			
Normal (%)	47.5	3.71±1.28	>4.0
Abnormal head (%)	36.5	75.14±4.45	–
Abnormal neck & midpiece (%)	33.0	60.09±2.69	–
Abnormal principal & end piece (%)	17.5	48.40±0.45	–
Sperm flagella[3]			
Morphologically normal (%)	81.3	27.35±1.58	>23.0
Absent (%)	1.5	13.04±1.37	<5.0
Bent (%)	4.4	4.72±0.35	<13.0
Coiled (%)	4.4	10.94±1.29	<17.0
Short (%)	5.4	10.78±2.92	<1.0
Irregular caliber (%)	2.5	28.45±2.56	<2.0
Double tails (%)	0.5	4.72±0.35	<1.0

Data are mean±SEM. “Age” and “Years of marriage” were counted to 2024. MT: c.916C>T. ND: Not determined. –: Not available. [1]: Reference values were suggested by the local clinical laboratory. [2]: Reference values are shown according to the WHO (World Health Organization, 2021). Headless or tailless sperm were excluded. [3]: According to MMAF standards. Reference values are shown according to fertile men from a previous report (Auger et al., 2016).

expression of *CCDC146* mRNA in the patient. The *CCDC146* mRNA band was observed in the peripheral blood of the patient (Supplementary Figure S6), suggesting that the mutant *CCDC146* transcript was not undergoing nonsense-mediated decay. Subsequently, WT and mutant human CCDC146 with N-terminal HA tags were expressed in HEK293T cells, followed by immunoblot analysis. The mutant protein was detected at the expected size (Figure 1F), suggesting that the *CCDC146* mutation might lead to the generation of a truncated protein. In summary, a homozygous nonsense mutation in *CCDC146* was identified in our patient, which potentially led to the generation of a truncated protein.

Impaired spermiogenesis in *Ccdc146* mutant mice

To validate the pathogenicity of the *CCDC146* mutation identified in our patient, a mutant mouse model (*Ccdc146*$^{mut/mut}$) was generated using CRISPR/Cas9 genome editing technology. A base transition from C to T was introduced at the c.982C>T position, homologous to the human mutation site, resulting in the premature termination of CCDC146 protein translation (p.Arg328*) (Supplementary Figure S7A). Similar to human CCDC146, the mouse CCDC146 protein also contains five coiled-coil domains, with the premature stop codon occurring in the second domain (Supplementary Figure S7A). The presence of the truncated CCDC146 protein (amino acids 1–327) with an N-terminal HA tag was confirmed in the cell lines (Figure 2A), and RT-PCR products of the *Ccdc146* transcript were detected in the testes of *Ccdc146*$^{mut/mut}$ mice (Supplementary Figure S7B). However, in contrast to the control, signals of the CCDC146-C antibody (targeting amino acids 848–977 of the mouse CCDC146 protein) were absent in the principal pieces of *Ccdc146*$^{mut/mut}$ sperm (Figure 2B). These findings suggest that *Ccdc146*$^{mut/mut}$ mice produce a truncated CCDC146 protein lacking three of the five coiled-coil domains, successfully mimicking the mutation observed in our patient.

To further investigate the impact of this nonsense mutation on CCDC146 function, the phenotypes of the *Ccdc146*$^{mut/mut}$ mice were examined. Both *Ccdc146*$^{WT/mut}$ and *Ccdc146*$^{mut/mut}$ mice exhibited normal growth, without obvious defects or premature death. Although *Ccdc146* mRNA was expressed in the lung (Supplementary Figure S5D), the morphology of cilia in the respiratory tracts of *Ccdc146*$^{WT/mut}$ and *Ccdc146*$^{mut/mut}$ mice exhibited no significant differences (Supplementary Figure S8). However, the *Ccdc146*$^{mut/mut}$ male mice were completely infertile, while the *Ccdc146*$^{WT/mut}$ mice and *Ccdc146*$^{mut/mut}$ female mice displayed normal fertility, despite the presence of *Ccdc146* mRNA and protein expression in the oviduct (Supplementary Figure S9). These observations strongly suggest that the CCDC146 mutation specifically impairs spermatogenesis.

The testes of *Ccdc146*$^{mut/mut}$ mice were similar in size to those of their control littermates (Supplementary Figure S10A). Additionally, the testis weights and testis-to-body

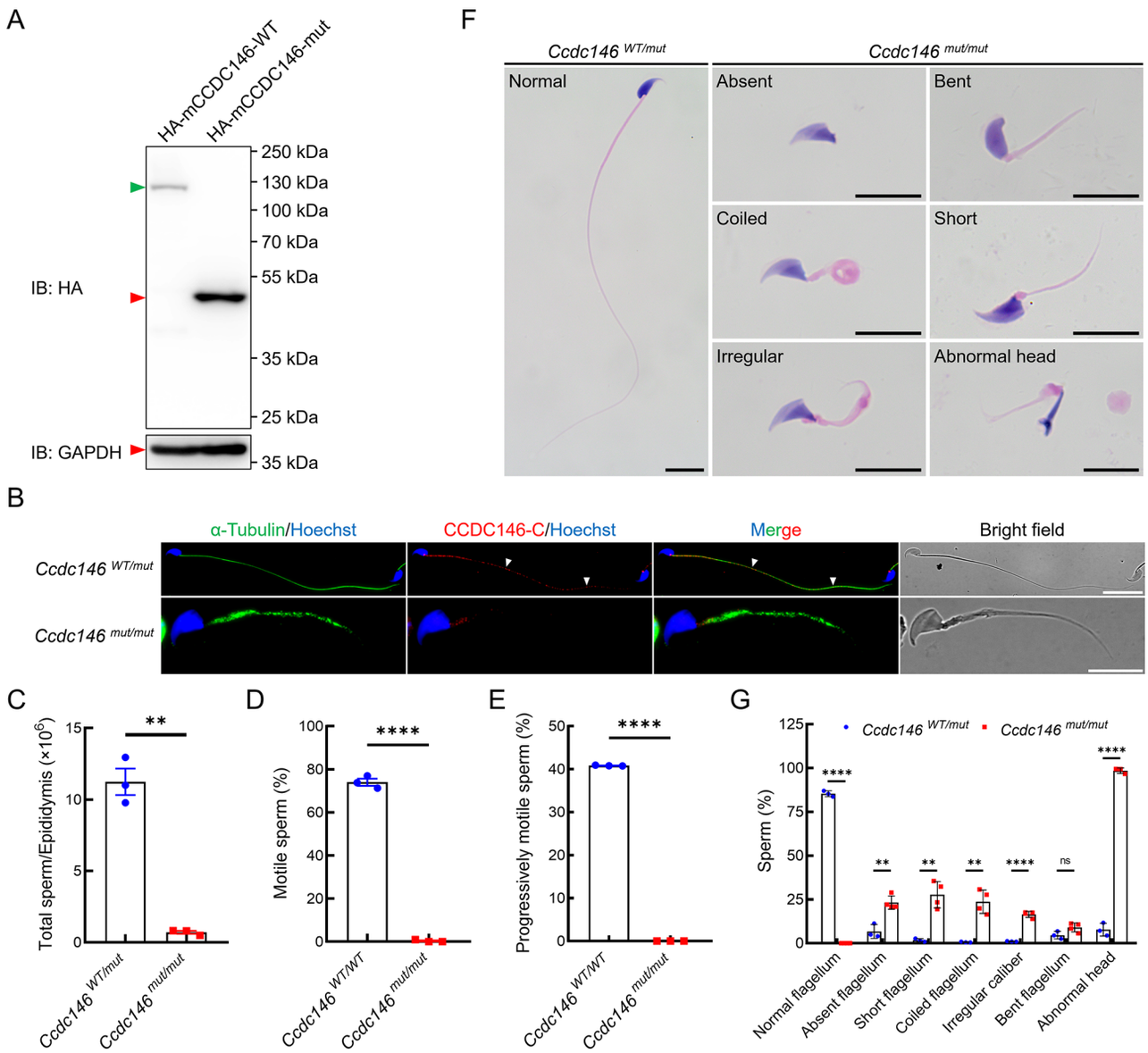

Figure 2 ***Ccdc146*$^{mut/mut}$ mice exhibited reduced sperm motility and malformed sperm heads and flagella**

A: Immunoblotting of HEK293T cells with anti-HA antibody after 24 h of expression of HA-tagged mouse CCDC146 proteins. Green and red arrowheads indicate normal and mutant proteins, respectively. GAPDH was used as the loading control. B: Representative images of sperm from *Ccdc146*$^{WT/mut}$ and *Ccdc146*$^{mut/mut}$ mice stained with anti-CCDC146-C antibody. Anti-α-tubulin antibody was used to mark microtubules. Arrowheads indicate specific signals along flagella of *Ccdc146*$^{WT/mut}$ sperm. Scale bars: 20 μm. C: Sperm counts per epididymis of each *Ccdc146*$^{WT/mut}$ or *Ccdc146*$^{mut/mut}$ mouse at 8 weeks of age. D, E: Total motility (D) and progressive motility (E) of sperm from WT and *Ccdc146*$^{mut/mut}$ mice determined by CASA. Data are mean±SEM. ****: P<0.0001. F: Representative images of sperm showing normal morphology from *Ccdc146*$^{WT/mut}$ mice, or multiple morphological abnormalities of sperm heads and flagella from *Ccdc146*$^{mut/mut}$ mice after H&E staining. Scale bars: 10 μm. G: Percentages of abnormal morphologies of sperm flagella and heads in *Ccdc146*$^{mut/mut}$ mice. Data are mean±SEM. For each mouse, more than 200 sperm were counted. ns: Not significant; **: P<0.01; ****: P<0.0001.

weight ratios were within normal ranges (Supplementary Figure S10B). However, sperm number in the epididymides of *Ccdc146*$^{mut/mut}$ mice was significantly reduced to approximately 10% of that in control mice (Figure 2C). Histological analysis of the cauda epididymides confirmed this reduction, revealing markedly fewer sperm and an increased amount of cell debris (Supplementary Figure S10C). The morphology of spermatocytes and round spermatids in the seminiferous tubules of *Ccdc146*$^{mut/mut}$ mice did not differ considerably from that of the control mice (Supplementary Figure S10C). However, misshapen nuclei in spermatids were first observed in Stage X–XI tubules (Steps 10–11), accompanied by narrow and symmetrical manchettes (Supplementary Figure S10D). These spermatids were significantly eliminated in Stage VII–VIII tubules (Steps 15–16) (Supplementary Figure S10C), suggesting that the reduction in sperm count was due to the elimination of elongated spermatids with abnormal nuclear shapes. Furthermore, nearly all sperm in the cauda epididymis of *Ccdc146*$^{mut/mut}$ mice were immotile, with only a few sperm exhibiting sluggish motility (Figure 2D, E). Sperm collected from the cauda epididymis of *Ccdc146*$^{mut/mut}$ mice exhibited multiple severe morphological defects, predominantly short flagella, which accounted for the highest percentage (26.7%) (Figure 2F, G). Furthermore, 98.5% of *Ccdc146*$^{mut/mut}$ sperm

displayed head malformations (Figure 2F, G). These findings highlight the presence of multiple morphological abnormalities in both sperm flagella and heads in *Ccdc146*$^{mut/mut}$ mice. The phenotypic similarities between the *Ccdc146*$^{mut/mut}$ mice and our patient strongly suggest that the nonsense mutation in *CCDC146* is pathogenic and contributes to male infertility.

Disruption of axonemal protein transportation in *Ccdc146*$^{mut/mut}$ spermatids

Given the axonemal localization of CCDC146 in human and mouse spermatozoa, the expression patterns of key axonemal proteins were examined in cauda epididymal sperm. Unlike the linear and continuous distribution observed along the entire axonemes in the control sperm, *Ccdc146*$^{mut/mut}$ sperm exhibited aberrant localizations of DNAH17, DNAH1, and SPAG6 around the axonemes (Figure 3A–C). Specifically, these proteins displayed reduced and scattered signals within the flagella, or were concentrated in coiled or twisted regions, instead of uniformly along the straight sections of the flagella (Figure 3A–C), indicating impaired assembly of outer dynein arms (ODAs), inner dynein arms (IDAs), and CPs in *Ccdc146*$^{mut/mut}$ sperm. Furthermore, the protein levels of several key flagellar components were significantly decreased in *Ccdc146*$^{mut/mut}$ sperm (Figure 3D; Supplementary Figure S11A). These findings suggest that the mutant CCDC146 protein likely disrupts the assembly of essential axonemal proteins. Notably, no significant decreases in the protein levels of these flagellar components were detected in *Ccdc146*$^{mut/mut}$ testes (Supplementary Figure S11B, C), implying that the disruption likely occurs during protein transport within spermatids, a fundamental process integral to the development of sperm flagella.

Considering that sperm mitochondria are isolated from the flagellar matrix by the annulus, a sperm-specific structure situated at the transition zone between the midpiece and principal piece (Avidor-Reiss et al., 2017), staining was conducted using Mito-Tracker Red (a mitochondrial marker) along with single antibodies of axonemal proteins to confirm disrupted protein transportation in the testicular spermatids of *Ccdc146*$^{mut/mut}$ mice. Compared to control spermatids, the linear signals of DNAH17, DNAH1, and SPAG6 were absent in the distal ends of the mutant flagella. Instead, these proteins exhibited diffuse signals accumulating in the cytoplasm, as marked by Mito-Tracker Red (Figure 4A–C). The accumulation of axonemal proteins in mitochondrion-containing cytoplasmic regions suggests that several flagellar proteins were insufficiently transported through the basal bodies or annuluses in *Ccdc146*$^{mut/mut}$ mice during spermiogenesis. This aberrant distribution implies that the mutant CCDC146 protein disrupts the proper localization of essential axonemal components within the sperm flagella, underscoring the crucial role of CCDC146 in the recruitment and maintenance of vital flagellar proteins in mammals.

Disruption of IFT20 localization and maintenance in *Ccdc146*$^{mut/mut}$ testes

During the development of sperm flagella, large complexes of axonemal proteins formed in the cytoplasm are continuously delivered to the basal body via the intramanchette transport (IMT) system. Subsequently, IFT trains transport these proteins to their respective destinations (Lehti & Sironen, 2016; Taschner & Lorentzen, 2016). IFT proteins are categorized into IFT-A proteins, responsible for retrograde movement, and IFT-B proteins, involved in anterograde transport (Taschner & Lorentzen, 2016). Within the IFT-B complex, IFT88 and IFT52 serve as the core, while IFT74 stabilizes the core in conjunction with IFT81. Additionally, IFT20 plays a critical role in stabilizing the connections

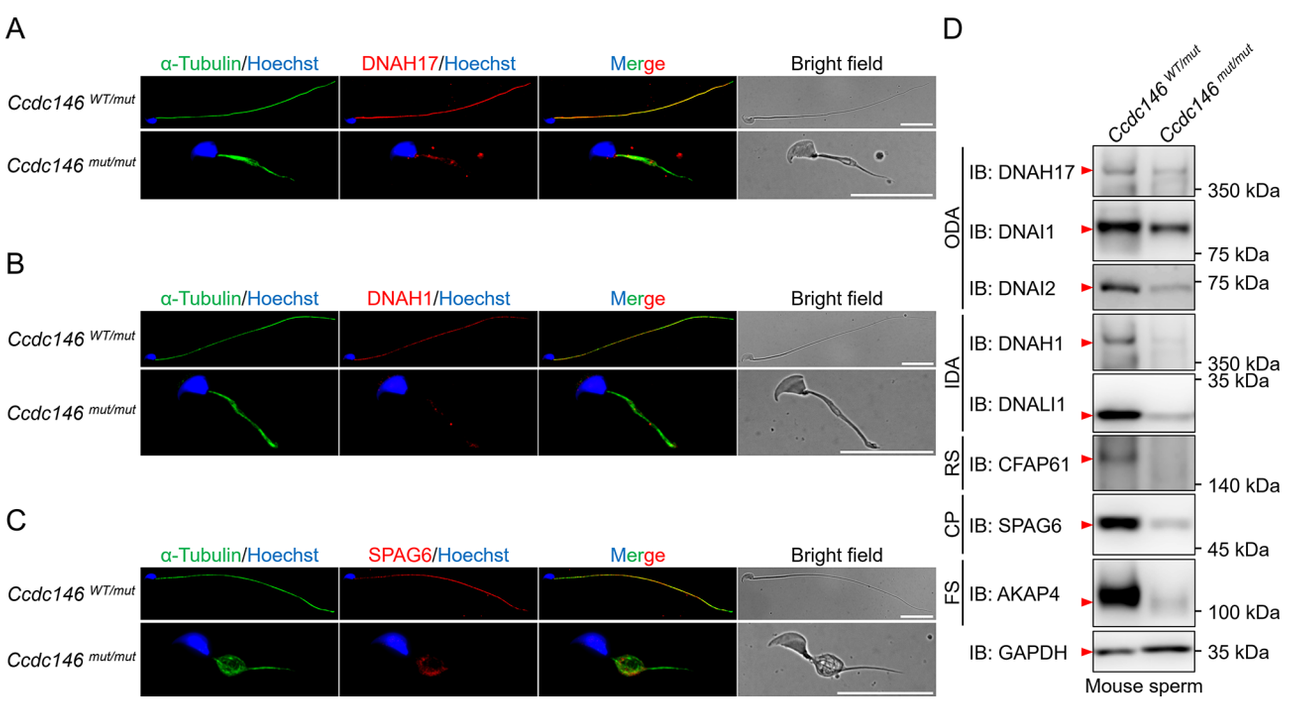

Figure 3 *Ccdc146*$^{mut/mut}$ mice exhibited impaired localizations and reduced levels of axonemal proteins in sperm

A–C: Representative images of sperm stained with anti-DNAH17 (A), anti-DNAH1 (B), or anti-SPAG6 (C) antibodies from *Ccdc146*$^{WT/mut}$ and *Ccdc146*$^{mut/mut}$ mice. Anti-α-tubulin antibody was used to mark microtubules. Scale bars: 20 μm. D: Immunoblotting of epididymal sperm from *Ccdc146*$^{WT/mut}$ and *Ccdc146*$^{mut/mut}$ mice with indicated antibodies. Red arrowheads indicate full-length proteins. GAPDH was used as the loading control. ODA, outer dynein arm; IDA, inner dynein arm; RS, radial spoke; CP, central pair; FS, fibrous sheath.

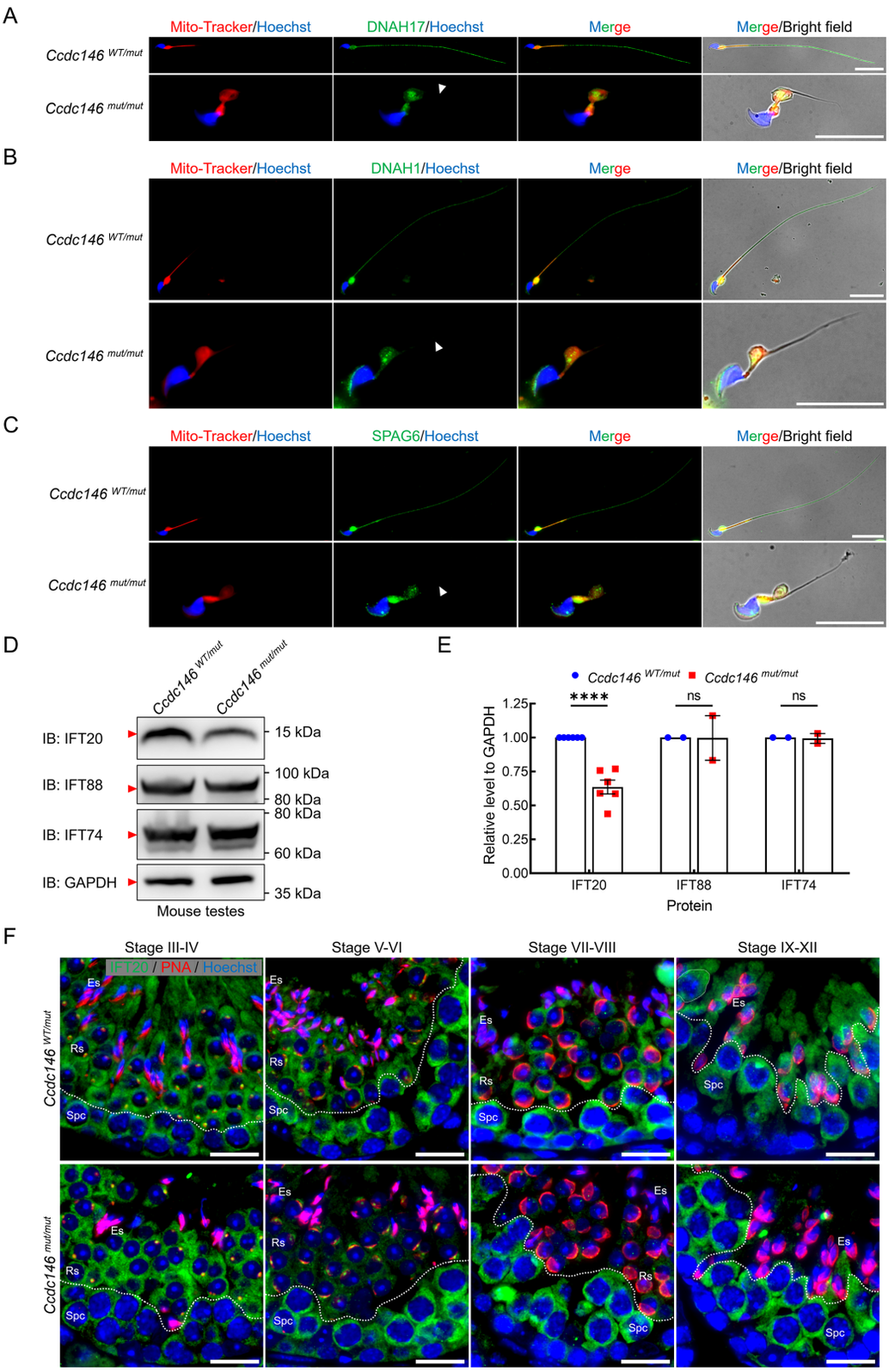

Figure 4 *Ccdc146*$^{mut/mut}$ spermatids showed impaired localization and maintenance of intraflagellar transport proteins

A–C: Representative images of spermatids stained with anti-DNAH17 (A), anti-DNAH1 (B), or anti-SPAG6 (C) antibodies from *Ccdc146*$^{WT/mut}$ and *Ccdc146*$^{mut/mut}$ mice. Mito-Tracker Red was used to label mitochondria in the cytoplasm or midpiece. Arrowheads show flagellar segments without signals of indicated proteins. Scale bars: 20 μm. D: Immunoblotting of testicular lysates from *Ccdc146*$^{WT/mut}$ and *Ccdc146*$^{mut/mut}$ mice with indicated antibodies. Red arrowheads indicate full-length proteins. GAPDH was used as the loading control. E: Relative band grayscales of IFT proteins to GAPDH in testicular lysates from *Ccdc146*$^{WT/mut}$ and *Ccdc146*$^{mut/mut}$ mice. Data are mean±SEM. ns: Not significant; ****: P<0.0001. F: Representative images of seminiferous tubule sections of *Ccdc146*$^{WT/mut}$ and *Ccdc146*$^{mut/mut}$ mice stained with anti-IFT20 antibody. Stages of seminiferous tubules were distinguished based on compositions of germ cells and arc angles of peanut agglutinin (PNA) signals in round spermatids. Dashed lines show regions of spermatids. Spc, spermatocyte; Rs, round spermatid; Es, elongating/elongated spermatid. Scale bars: 50 μm.

between adjacent IFT-B repeats along with IFT54 (Lacey et al., 2023; Wang et al., 2022a). To determine whether deficient protein distribution in *Ccdc146*$^{mut/mut}$ spermatids was due to impaired IMT/IFT protein function, we investigated the protein levels of IFT20, IFT74, and IFT88 in the testes of *Ccdc146*$^{mut/mut}$ mice. Although the protein levels of IFT74 and IFT88 remained unchanged, there was a notable reduction (approximately 40%) in the protein content of IFT20 in the mutant testes (Figure 4D, E). The dynamic localization patterns of IFT20 in male germ cells at various developmental stages were further compared. In the seminiferous tubules of control mice, IFT20 signals were enriched in the cytoplasm of spermatocytes and round spermatids (Figure 4F). During spermiogenesis, IFT20 was recruited to form bright foci at the centers of acrosomes in round spermatids from Steps 3 to 6 (Stage III–VI tubules) and moved toward the lumen in elongating spermatid cytoplasm during Steps 9 to 12 (Stage IX–XII tubules), with slightly stronger signals along the lateral sides of the nuclei, resembling the microtubule bundles of the manchette (Figure 4F). In the seminiferous tubules of *Ccdc146*$^{mut/mut}$ mice, the localization and intensity of IFT20 signals remained unaffected in the spermatocytes and bright foci at the centers of acrosomes in Step 3 to 6 round spermatids (Stage III–VI tubules) (Figure 4F). However, the IFT20 signals in the cytoplasm of mutant spermatids diminished at Steps 5 to 6 (Stage V–VI tubules), just prior to manchette formation (Figure 4F). Subsequently, IFT20 signals in the manchette were significantly weakened or even absent in mutant spermatids during Steps 9 to 12 (Stage IX–XII tubules) (Figure 4F). These findings suggest an abnormal recruitment of the IFT20 protein into the manchette, potentially impeding the transportation of flagellar proteins.

To assess whether the *Ccdc146* mutation disrupted the recruitment of other IFT members, immunostaining for IFT74 and IFT88 was conducted to investigate their localization in spermatids. In control spermatids, IFT74 and IFT88 were localized along the growing flagella and posterior part of the manchette during Steps 9 to 12 (Stage IX–XII tubules). However, in *Ccdc146*$^{mut/mut}$ spermatids, the signals for both IFT74 and IFT88 were diffusely distributed around the nuclei, without co-localization with manchette microtubules (Supplementary Figure S12), indicating a failure in the recruitment of IFT74 and IFT88 in mutant spermatids. These results suggest that impaired IMT/IFT processes in *Ccdc146*$^{mut/mut}$ spermatids, as evidenced by the inadequate maintenance and deficient localization of IFT20, may further contribute to the variations in axonemal protein content in the sperm of *Ccdc146*$^{mut/mut}$ mice.

C terminus of CCDC146 is required for interaction with IFT20

To investigate the associations between CCDC146 and IFT20, HEK293T cells were co-transfected with plasmids expressing HA-tagged mouse CCDC146 and GFP-tagged mouse IFT20 proteins. Immunoprecipitation using anti-GFP beads revealed the presence of full-length CCDC146 protein (Figure 5A), suggesting a possible interaction between IFT20 and CCDC146 in control mice. However, when the mutant CCDC146 protein was co-expressed with the IFT20 protein, the truncated CCDC146 protein (amino acids 1–327) was only detected in the input samples and not in the IFT20 pull-down products (Figure 5A), indicating a loss of interaction between mutant CCDC146 and IFT20 in *Ccdc146*$^{mut/mut}$ mice. Similarly, full-length human CCDC146 interacted with human IFT20, but the truncated human CCDC146 protein (amino acids 1–305) did not (Figure 5B). This loss of interaction was also reflected by reduced and mislocalized IFT20 signals in the sperm of our patient (Figure 5C), suggesting that the *CCDC146* mutation impairs IFT in human sperm by destroying its interaction with IFT20.

To determine whether insufficient IFT20 protein along the sperm flagella contributed to aberrant localizations of axonemal proteins in a manner similar to *Ccdc146*$^{mut/mut}$ mice, staining of DNAH17, DNAH1, and SPAG6 was performed on the patient's sperm. The signal intensities of DNAH17 and DNAH1 along the sperm flagella were decreased (Figure 5D, E), while SPAG6 signals were comparable between the patient and fertile control (Supplementary Figure S13). This suggests that DNAH17 and DNAH1 localization is affected by *CCDC146* deficiency in our patient, similar to the observations in *Ccdc146*$^{mut/mut}$ mice. In summary, CCDC146 is essential for maintaining IFT20 levels and facilitating the transport and organization of flagellar proteins, such as DNAH17, DNAH1, and SPAG6, along the axoneme during spermiogenesis (Figure 6).

DISCUSSION

In this study, a novel homozygous nonsense mutation in *CCDC146* (c.916C>T, p.Arg306*) was identified in an infertile man diagnosed with OAT, who was born to first-cousin parents. To confirm the pathogenicity of the *CCDC146* nonsense mutation, a mouse model harboring the same mutation was generated, which exhibited similar abnormalities in sperm counts, morphology, and motility, indicating that the *CCDC146* c.916C>T mutation is deleterious and associated with male infertility. Further analysis revealed the production of truncated CCDC146 in both the patient and the *Ccdc146*$^{mut/mut}$ mice, resulting in the loss of interaction with IFT20. This disruption likely affects axonemal protein transport and localization, leading to abnormal spermiogenesis.

Pathogenicity and effects of *CCDC146* mutations

CCDC146 is highly expressed in human testis (Supplementary Figure S5A, B). A recent study identified two homozygous mutations in *CCDC146* (c.1084C>T and c.2112del) in two MMAF patients, who exhibited asthenoteratozoospermia with normal sperm counts (Muroňová et al., 2024), linking *CCDC146* mutations to human sperm malformations. However, our patient, harboring a novel *CCDC146* nonsense mutation (c.916C>T), exhibited a severely decreased sperm count in addition to similar sperm deformities, particularly irregular tails (Table 1). This suggests that *CCDC146* mutations can also cause OAT in humans, expanding the phenotypic profile of such mutations and reflecting the complexity of underlying genetic backgrounds.

The phenotypic variations observed in different patients with *CCDC146* mutations may be due to the different functions of residual CCDC146 proteins. Although the presence of truncated CCDC146 protein was not evaluated in the above-described patients with the two mutations (Muroňová et al., 2024), our study clearly demonstrated the presence of the *CCDC146* transcript in the blood of our patient (Supplementary Figure S6). Additionally, the expression level of the truncated CCDC146 protein in HEK293T cells was comparable to that of the full-length CCDC146 protein (Figure 1F), suggesting a high likelihood of the existence of

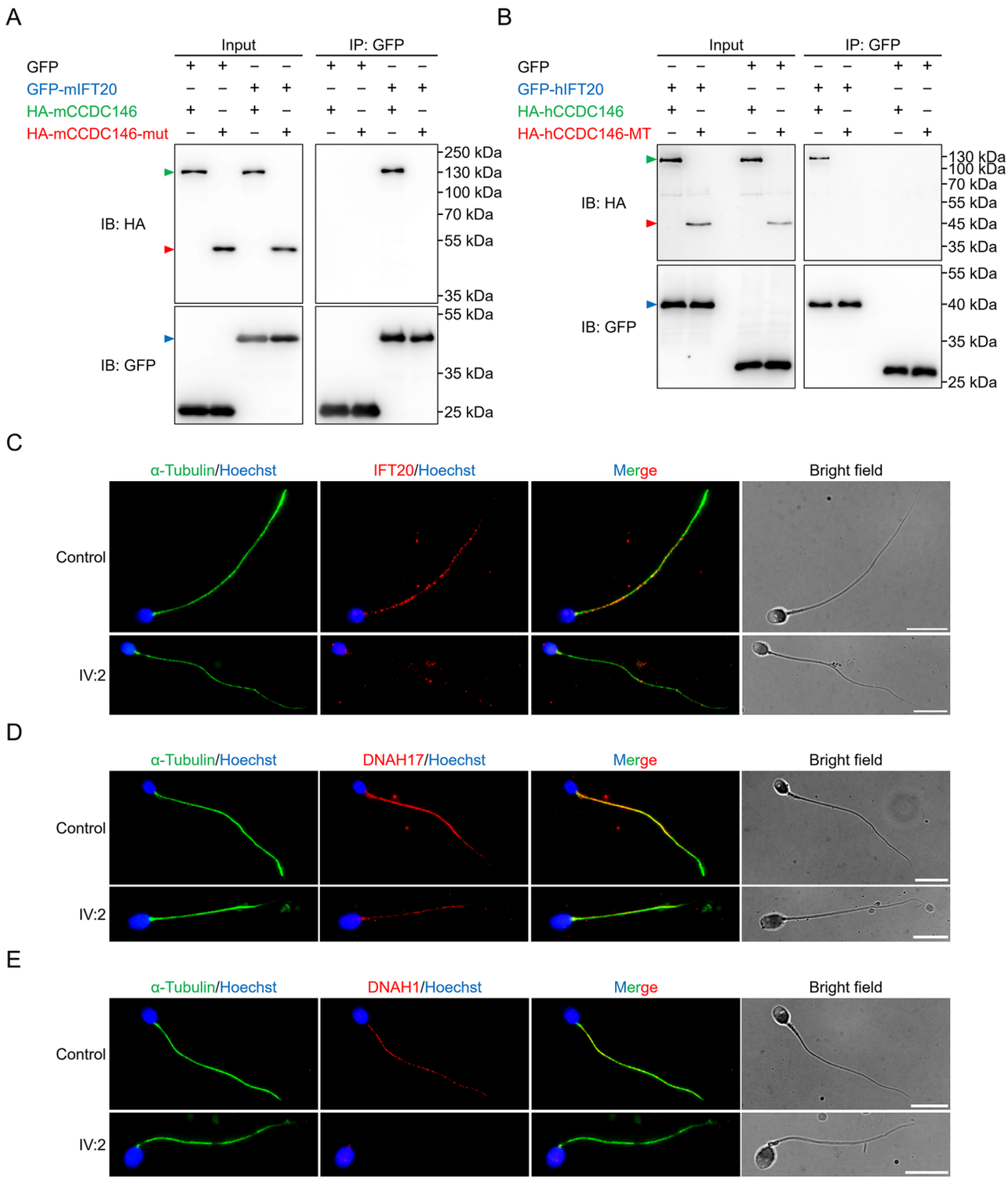

Figure 5 C terminus of CCDC146 was essential for IFT20 interaction and flagellar protein localization on human sperm

A, B: Co-IP of interaction between mouse (A) or human (B) IFT20 protein (fused with N-terminal GFP tag) and mouse (A) or human (B) CCDC146 full-length or truncated protein (fused with N-terminal HA tag) exogenously expressed in HEK293T cells. Arrowheads indicate recombinant proteins of corresponding colors. C–E: Representative images of sperm stained with anti-IFT20 (C), anti-DNAH17 (D), or anti-DNAH1 (E) antibodies from IV:2 and fertile control. Anti-α-tubulin antibody was used to mark microtubules. Scale bars: 10 μm.

truncated CCDC146 protein in the patient's testes. Furthermore, the *Ccdc146*$^{mut/mut}$ mice, designed to mimic both the type and effect of the *CCDC146* mutation, displayed *Ccdc146* mRNA expression in mutant testes and oviducts (Supplementary Figures S7B, S9B). A higher level of truncated mouse CCDC146 protein was also observed in HEK293T cells (Figure 2A). The close replication of the effects of the mutation and the similar OAT phenotypes observed in both our patient and *Ccdc146*$^{mut/mut}$ mice suggest that the impact of the *CCDC146* mutation on protein expression is consistent across species. This underscores the importance of using mutation-mimicking animal models in pathogenicity studies and confirms that mutations in *CCDC146* can cause OAT-associated infertility in humans.

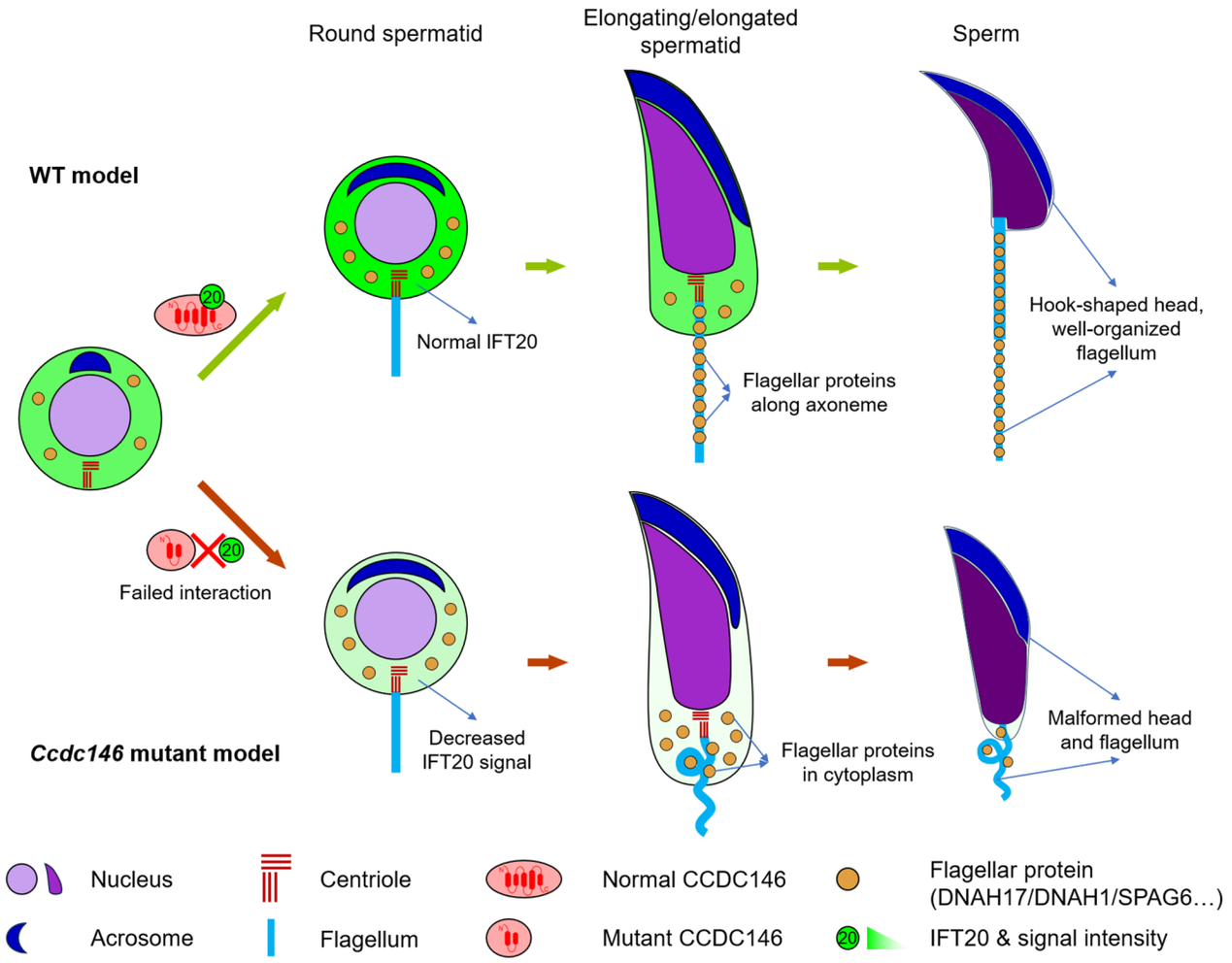

Figure 6 Schematic of the potential mechanism by which *Ccdc146* deficiency causes male infertility

In WT mice, CCDC146 interacts with IFT20, facilitating transport and organization of flagellar proteins, such as DNAH17, DNAH1, and SPAG6, along the axoneme. However, in *Ccdc146*$^{mut/mut}$ mice, truncated CCDC146 protein fails to interact with IFT20, resulting in decreased IFT20 signals from round to elongated spermatids, leading to a reduction in flagellar proteins within sperm and malformations of sperm heads and tails (Zhang et al., 2016).

Localization patterns of CCDC146

CCDC146 was initially identified as a centrosomal protein, found at the centrioles of bovine sperm and at mother centrioles in HeLa and RPE1 cells when overexpressed (Firat-Karalar et al., 2014). Recent studies confirmed its centriolar or centrosomal localization in somatic cells, as well as in round spermatids and elongating spermatids (Ma et al., 2024; Muroňová et al., 2024). However, Muroňová et al. (2024) suggested that in human and mouse ejaculated spermatozoa, CCDC146 is exclusively localized along the flagellar principal piece, rather than co-localizing with Centrin at the centrioles. In this study, we confirmed that CCDC146 is localized along the flagella of human and mouse ejaculated spermatozoa, as indicated by specific signals of the CCDC146-C antibody within the principal piece in control sperm (Figures 1E, 2B). The absence of CCDC146 localization in sperm centrioles may be due to the reutilization of centrosomal proteins in axonemes during spermiogenesis (Muroňová et al., 2024). Moreover, CCDC146 has been observed in the mitotic spindles, including kinetochores and midbodies, of dividing cells, with its presence significantly enhanced when microtubule integrity is disrupted by sarkosyl detergent (Muroňová et al., 2024). These observations, combined with the strong interaction between CCDC146 and α/β tubulins in the mouse testis (Ma et al., 2024), suggest that CCDC146 is a potential microtubule-associated protein (MAP). Thus, we propose that CCDC146 exhibits dynamic localization patterns during spermiogenesis in humans and mice, initially appearing on centrioles and migrating to axonemes during sperm elongation. These dynamic localizations are similar to those observed in other MMAF-associated proteins, like CFAP53 and CCDC38, whose localizations shift from centrioles to manchettes and ultimately to sperm flagella during spermiogenesis (Wu et al., 2021; Zhang et al., 2022).

IFT20 as a potential key partner of CCDC146

The expression levels of several key axonemal proteins, including DNAH17 (ODA), DNAH1 (IDA), and SPAG6 (CP), were comparable between the control and *Ccdc146*$^{mut/mut}$ mice in testicular tissue, but were significantly reduced in ejaculated sperm (Figure 3D; Supplementary Figure S11). These proteins were exclusively retained in the cytoplasm of mutant spermatids, as indicated by Mito-Tracker Red signals (Figure 4A–C), likely leading to their subsequent mislocalization in *Ccdc146*$^{mut/mut}$ sperm flagella (Figure 3). These defects suggest a deficiency in the protein transportation system within spermatids.

Regarding the components of the protein transportation system, we observed mislocalization of IFT74 and IFT88 in the manchettes of *Ccdc146*$^{mut/mut}$ spermatids (Supplementary Figure S12). Notably, a decrease in IFT20 signals was detected in the cytoplasm of round spermatids during Steps 5–6 (Figure 4F), prior to manchette assembly and the subsequent recruitment of IFT74 and IFT88. Although recent studies have reported interactions between mouse CCDC146 and both IFT20 and IFT88 (Ma et al., 2024), our findings indicated that the interaction between mouse CCDC146 and IFT20 was stronger than that with IFT88 (Supplementary Figure S14), with both interactions completely disrupted by the truncated CCDC146 protein (Figure 5A; Supplementary Figure S14). These results suggest that IFT20 is a key partner of CCDC146 during spermiogenesis.

The higher conservation of the C-terminal amino acid sequences of CCDC146 across vertebrates implies that this region performs essential functions, while the N-terminal region only contains a PF05557 motif (amino acids 130–162 in mouse CCDC146), which may facilitate the binding of CCDC146 to microtubular structures in somatic cells (Muroňová et al., 2024). While *Ccdc146* knockout mice reportedly show significantly reduced levels of both IFT20 and IFT88 in their testes, the *Ccdc146*$^{mut/mut}$ mice, which produced a truncated N-terminal protein, showed reduced levels of IFT20 only. These results suggest that CCDC146-IFT20 interactions are conserved across humans and mice and that the C-terminal coiled-coils of CCDC146 play a crucial role in maintaining IFT20 expression and localization during spermiogenesis (Figure 6).

Potential role of CCDC146 in axonemal microtubule maintenance

As a potential MAP, CCDC146 may play a crucial role in the assembly and structural integrity of sperm flagella (Ma et al., 2024). Expansion microscopy has shown significant overlap of CCDC146 signals with MTDs along sperm flagella (Muroňová et al., 2024), suggesting involvement in the construction of functional MTDs. CCDC146 has also been found to interact with TEKT2 and SPACA9, two well-studied microtubule inner proteins (MIPs) that specifically reside within the lumen of MTDs (Ma et al., 2024), further supporting its tight association with these structural components.

Previous transmission electron microscopy studies have revealed either severely disorganized “9+2” structures filled with ODFs or classic “9+2” structures with extra ODFs in *Ccdc146*-deleted sperm (Ma et al., 2024; Muroňová et al., 2024). CCDC146 does not directly interact with any ODF scaffold proteins (ODF1–4), but does interact with CCDC38 and CCDC42, which are involved in ODF assembly (Ma et al., 2024; Tapia Contreras & Hoyer-Fender, 2019; Zhang et al., 2022). Thus, the excessive presence of ODFs in sperm flagella observed in previous studies (Ma et al., 2024; Muroňová et al., 2024) is likely an indirect effect of CCDC146 deletion. Another possible explanation is the dissolution and degradation of sperm axonemal microtubules, as indicated by the discontinuous tubulin signals based on immunofluorescence (Figures 2B, 3A–C). Despite almost equal amounts of total sperm protein in both the control and *Ccdc146*$^{mut/mut}$ mice (validated by InstaBlue Protein Stain), western blot analysis showed a marked decrease in tubulin levels in *Ccdc146*$^{mut/mut}$ mice, while GAPDH levels remained comparable to levels in the control mice (Supplementary Figure S15). These results suggest instability of sperm axonemal microtubules in *Ccdc146*$^{mut/mut}$ mice. *Ccdc146* knockout spermatids also exhibit abnormalities in other microtubular structures, such as over-elongated manchettes and supernumerary centrioles (Muroňová et al., 2024), further indicating that CCDC146 may be involved in the regulation of axonemal microtubules.

Dispensable role of CCDC146 in motile cilia

Because flagella and motile cilia share a similar “9+2” core axonemal structure, it is expected that key MAPs in sperm flagella, such as CCDC39, CCDC40, and CFAP57, also play essential roles in motile cilia, with mutations causing PCD-related symptoms (Blanchon et al., 2012; Bustamante-Marin et al., 2020; Walton et al., 2023). However, the *Ccdc146*$^{mut/mut}$ mice in our study exhibited normal growth, with no premature death or PCD-related symptoms, such as hydrocephalus, and with females displaying normal fertility (Supplementary Figure S9A), as also found in *Ccdc146* knockout mice (Ma et al., 2024). Similarly, no PCD-associated symptoms have been reported in patients with *CCDC146* mutations (Muroňová et al., 2024), and no studies have yet reported on infertile females with homozygous *CCDC146* mutations. These results suggest that CCDC146 is dispensable for the function of motile cilia across species, highlighting the need for further investigation into the underlying mechanisms.

Limitations of this study

This study has several limitations. First, despite extensive efforts to identify suitable antibodies (Supplementary Figure S16), the lack of an antibody capable of recognizing the N-terminal region of the human and mouse CCDC146 protein hindered the direct confirmation of the truncated CCDC146 protein *in vivo*. Although mass spectrometry could theoretically identify truncated CCDC146 protein fragments, the efficacy of this method remains uncertain. Second, the lack of appropriate methods made it difficult to monitor the earliest changes in *Ccdc146*$^{mut/mut}$ testicular cells, which requires a detailed interaction profile of CCDC146 and direct validation using effective antibodies. Therefore, the detailed functions of the N-terminal and C-terminal regions of CCDC146 need further study. Third, the limited availability of semen samples from the patient and his low sperm count restricted the acquisition of more data, such as western blot analyses, to detect alterations in the levels of flagellar proteins, as observed in the *Ccdc146*$^{mut/mut}$ mice.

The phenotypic similarities observed in the *CCDC146*-mutated infertile man and *Ccdc146*$^{mut/mut}$ mice suggest that the nonsense mutation in *CCDC146* is responsible for OAT and male sterility in both humans and mice. These findings emphasize the pivotal roles of CCDC146 in the development of sperm heads and tails, advancing our understanding of the etiology and pathology of sperm deficiencies. Furthermore, *CCDC146* could be included in mutation screening and genetic diagnosis for OAT-associated male infertility.

DATA AVAILABILITY

The raw sequence data reported in this paper have been deposited in the Genome Sequence Archive (GSA) in the National Genomics Data Center and China National Center for Bioinformation (https://ngdc.cncb.ac.cn/gsa-human; accession number HRA007703), Science Data Bank (DOI: 10.57760/sciencedb.j00139.00081), and NCBI Sequence Read Archive (SRA; https://www.ncbi.nlm.nih.gov/sra; BioProjectID PRJNA1158214). All other data supporting the findings of this study are available from the corresponding author upon reasonable request.

SUPPLEMENTARY DATA

Supplementary data to this article can be found online.

COMPETING INTERESTS

The authors declare that they have no competing interests.

AUTHORS' CONTRIBUTIONS

B.L.S., H.Z., and Q.H.S. designed and supervised the study. T.A., G.M., and B.L.S. collected the samples. J.W.Y., T.A., J.C., and B.L.S. performed the experiments. J.W.Y., T.A., J.T.Z., J.C., M.L.Y., X.H.H., and H.Z. analyzed the data. J.W.Y. wrote the manuscript. B.L.S., A.M., Q.H.S., H.M., and B.X. revised the manuscript. All authors read and approved the final version of the manuscript.

ACKNOWLEDGMENTS

The authors thank all the participants for their cooperation and all lab members for their experimental assistance. We thank Ranjha Khan for assisting with sample collection. We thank Prof. Wei Li and his lab member Yanjie Ma from the Guangzhou Women and Children's Medical Center for kindly providing antibodies and plasmids. We thank Li Wang and Dandan Song from the Center of Cryo-Electron Microscopy, Zhejiang University, for their technical assistance with transmission and scanning electron microscopy, respectively. We also thank the Bioinformatics Center of the University of Science and Technology of China, School of Life Sciences, for providing supercomputing resources.

REFERENCES

Agarwal A, Baskaran S, Parekh N, et al. 2021. Male infertility. *The Lancet*, **397**(10271): 319–333.

Auger J, Jouannet P, Eustache F. 2016. Another look at human sperm morphology. *Human Reproduction*, **31**(1): 10–23.

Avidor-Reiss T, Ha A, Basiri ML. 2017. Transition zone migration: a mechanism for cytoplasmic ciliogenesis and postaxonemal centriole elongation. *Cold Spring Harbor Perspectives in Biology*, **9**(8): a028142.

Blanchon S, Legendre M, Copin B, et al. 2012. Delineation of *CCDC39/CCDC40* mutation spectrum and associated phenotypes in primary ciliary dyskinesia. *Journal of Medical Genetics*, **49**(6): 410–416.

Bustamante-Marin XM, Horani A, Stoyanova M, et al. 2020. Mutation of CFAP57, a protein required for the asymmetric targeting of a subset of inner dynein arms in *Chlamydomonas*, causes primary ciliary dyskinesia. *PLoS Genetics*, **16**(8): e1008691.

Chang TL, Tang HY, Zhou X, et al. 2023. A novel homozygous nonsense variant of *AK7* is associated with multiple morphological abnormalities of the sperm flagella. *Reproductive Biomedicine Online*, **48**(5): 103765.

Chen DJ, Liang Y, Li J, et al. 2021. A novel *CCDC39* mutation causes multiple morphological abnormalities of the flagella in a primary ciliary dyskinesia patient. *Reproductive Biomedicine Online*, **43**(5): 920–930.

Cong JS, Wang X, Amiri-Yekta A, et al. 2022. Homozygous mutations in *CCDC34* cause male infertility with oligoasthenoteratozoospermia in humans and mice. *Journal of Medical Genetics*, **59**(7): 710–718.

Fan SX, Jiao YY, Khan R, et al. 2021. Homozygous mutations in *C14orf39/SIX6OS1* cause non-obstructive azoospermia and premature ovarian insufficiency in humans. *The American Journal of Human Genetics*, **108**(2): 324–336.

Fassad MR, Rumman N, Junger K, et al. 2023. Defective airway intraflagellar transport underlies a combined motile and primary ciliopathy syndrome caused by *IFT74* mutations. *Human Molecular Genetics*, **32**(21): 3090–3104.

Finetti F, Onnis A, Baldari CT. 2022. IFT20: an eclectic regulator of cellular processes beyond intraflagellar transport. *International Journal of Molecular Sciences*, **23**(20): 12147.

Firat-Karalar EN, Sante J, Elliott S, et al. 2014. Proteomic analysis of mammalian sperm cells identifies new components of the centrosome. *Journal of Cell Science*, **127**(19): 4128–4133.

Gong CJ, Abbas T, Muhammad Z, et al. 2022. A homozygous loss-of-function mutation in *MSH5* abolishes MutSγ axial loading and causes meiotic arrest in NOA-affected individuals. *International Journal of Molecular Sciences*, **23**(12): 6522.

Lacey SE, Foster HE, Pigino G. 2023. The molecular structure of IFT-A and IFT-B in anterograde intraflagellar transport trains. *Nature Structural & Molecular Biology*, **30**(5): 584–593.

Lehti MS, Sironen A. 2016. Formation and function of the manchette and flagellum during spermatogenesis. *Reproduction*, **151**(4): R43–R54.

Li H. 2013. Aligning sequence reads, clone sequences and assembly contigs with BWA-MEM. *arXiv*, doi: https://doi.org/10.48550/arXiv.1303.3997.

Liu H, Li W, Zhang Y, et al. 2017. IFT25, an intraflagellar transporter protein dispensable for ciliogenesis in somatic cells, is essential for sperm flagella formation. *Biology of Reproduction*, **96**(5): 993–1006.

Liu W, Wang YW, Zhang H, et al. 2022. Computationally predicted pathogenic *USP9X* mutation identified in infertile men does not affect spermatogenesis in mice. *Zoological Research*, **43**(2): 225–228.

Liu Z, Yan WW, Liu SH, et al. 2023. Regulatory network and targeted interventions for CCDC family in tumor pathogenesis. *Cancer Letters*, **565**: 216225.

Lu S, Gu YY, Wu YF, et al. 2021. Bi-allelic variants in human *WDR63* cause male infertility via abnormal inner dynein arms assembly. *Cell Discovery*, **7**(1): 110.

Ma A, Zeb A, Ali I, et al. 2022a. Biallelic variants in *CFAP61* cause multiple morphological abnormalities of the flagella and male infertility. *Frontiers in Cell and Developmental Biology*, **9**: 803818.

Ma A, Zhou JT, Ali H, et al. 2023. Loss-of-function mutations in *CFAP57* cause multiple morphological abnormalities of the flagella in humans and mice. *JCI Insight*, **8**(3): e166869.

Ma H, Li T, Xie XF, et al. 2022b. RAD51AP2 is required for efficient meiotic recombination between X and Y chromosomes. *Science Advances*, **8**(2): eabk1789.

Ma H, Zhang BB, Khan A, et al. 2021. Novel frameshift mutation in *STK33* is associated with asthenozoospermia and multiple morphological abnormalities of the flagella. *Human Molecular Genetics*, **30**(21): 1977–1984.

Ma YJ, Wu BB, Chen YH, et al. 2024. CCDC146 is required for sperm flagellum biogenesis and male fertility in mice. *Cellular and Molecular Life Sciences*, **81**(1): 1.

Muroňová J, Kherraf ZE, Giordani E, et al. 2024. Lack of CCDC146, a ubiquitous centriole and microtubule-associated protein, leads to non-syndromic male infertility in human and mouse. *eLife*, **12**: RP86845.

Narasimhan V, Danecek P, Scally A, et al. 2016. BCFtools/RoH: a hidden Markov model approach for detecting autozygosity from next-generation sequencing data. *Bioinformatics*, **32**(11): 1749–1751.

Njagi P, Groot W, Arsenijevic J, et al. 2023. Financial costs of assisted reproductive technology for patients in low- and middle-income countries: a systematic review. *Human Reproduction Open*, **2023**(2): hoad007.

Pazour GJ, Agrin N, Leszyk J, et al. 2005. Proteomic analysis of a eukaryotic cilium. *The Journal of Cell Biology*, **170**(1): 103–113.

Pazour GJ, Rosenbaum JL. 2002. Intraflagellar transport and cilia-dependent diseases. *Trends in Cell Biology*, **12**(12): 551–555.

Pedersen BS, Quinlan AR. 2017. Who's who? Detecting and resolving sample anomalies in human DNA sequencing studies with *Peddy*. *The American Journal of Human Genetics*, **100**(3): 406–413.

Priyanka PP, Yenugu S. 2021. Coiled-coil domain-containing (CCDC) proteins: functional roles in general and male reproductive physiology. *Reproductive Sciences*, **28**(10): 2725–2734.

San Agustin JT, Pazour GJ, Witman GB. 2015. Intraflagellar transport is essential for mammalian spermiogenesis but is absent in mature sperm. *Molecular Biology of the Cell*, **26**(24): 4358–4372.

Sang Q, Ray PF, Wang L. 2023. Understanding the genetics of human infertility. *Science*, **380**(6641): 158–163.

Schmidts M, Frank V, Eisenberger T, et al. 2013. Combined NGS approaches identify mutations in the intraflagellar transport gene *IFT140* in skeletal ciliopathies with early progressive kidney disease. *Human Mutation*, **34**(5): 714–724.

Sha YW, Wang X, Yuan JT, et al. 2020. Loss-of-function mutations in centrosomal protein 112 is associated with human acephalic spermatozoa phenotype. *Clinical Genetics*, **97**(2): 321–328.

Shaheen R, Alsahli S, Ewida N, et al. 2020. Biallelic mutations in tetratricopeptide repeat domain 26 (*Intraflagellar Transport 56*) cause severe biliary ciliopathy in humans. *Hepatology*, **71**(6): 2067–2079.

Shi BL, Shah W, Liu L, et al. 2023. Biallelic mutations in RNA-binding protein ADAD2 cause spermiogenic failure and non-obstructive azoospermia in humans. *Human Reproduction Open*, **2023**(3): hoad022.

Tapia Contreras C, Hoyer-Fender S. 2019. CCDC42 localizes to manchette, HTCA and tail and interacts with ODF1 and ODF2 in the formation of the male germ cell cytoskeleton. *Frontiers in Cell and Developmental Biology*, **7**: 151.

Taschner M, Lorentzen E. 2016. The intraflagellar transport machinery. *Cold Spring Harbor Perspectives in Biology*, **8**(10): a028092.

Tian SX, Tu CF, He XJ, et al. 2023. Biallelic mutations in *CFAP54* cause male infertility with severe MMAF and NOA. *Journal of Medical Genetics*, **60**(8): 827–834.

Touré A, Martinez G, Kherraf ZE, et al. 2021. The genetic architecture of morphological abnormalities of the sperm tail. *Human Genetics*, **140**(1): 21–42.

Walton T, Gui M, Velkova S, et al. 2023. Axonemal structures reveal mechanoregulatory and disease mechanisms. *Nature*, **618**(7965): 625–633.

Wang JL, Zhu X, Wang ZM, et al. 2022a. Assembly and stability of IFT-B complex and its function in BBSome trafficking. *iScience*, **25**(12): 105493.

Wang JX, Wang WZ, Shen LY, et al. 2022b. Clinical detection, diagnosis and treatment of morphological abnormalities of sperm flagella: a review of literature. *Frontiers in Genetics*, **13**: 1034951.

Wang K, Li MY, Hakonarson H. 2010. ANNOVAR: functional annotation of genetic variants from high-throughput sequencing data. *Nucleic Acids Research*, **38**(16): e164.

Wellard SR, Hopkins J, Jordan PW. 2018. A seminiferous tubule squash technique for the cytological analysis of spermatogenesis using the mouse model. *Journal of Visualized Experiments*, (132): 56453.

World Health Organization. 2021. WHO Laboratory Manual for the Examination and Processing of Human Semen. 6th ed. Geneva: WHO.

Wu BB, Yu XC, Liu C, et al. 2021. Essential role of CFAP53 in sperm flagellum biogenesis. *Frontiers in Cell and Developmental Biology*, **9**: 676910.

Xu JZ, Gao JN, Liu JY, et al. 2022. ZFP541 maintains the repression of pre-pachytene transcriptional programs and promotes male meiosis progression. *Cell Reports*, **38**(12): 110540.

Yang C, Lin XQ, Ji ZY, et al. 2022. Novel bi-allelic variants in *KASH5* are associated with meiotic arrest and non-obstructive azoospermia. *Molecular Human Reproduction*, **28**(7): gaac021.

Yin H, Ma H, Hussain S, et al. 2019. A homozygous *FANCM* frameshift pathogenic variant causes male infertility. *Genetics in Medicine*, **21**(1): 62–70.

Zhang BB, Ma H, Khan T, et al. 2020. A *DNAH17* missense variant causes flagella destabilization and asthenozoospermia. *The Journal of Experimental Medicine*, **217**(2): e20182365.

Zhang RD, Wu BB, Liu C, et al. 2022. CCDC38 is required for sperm flagellum biogenesis and male fertility in mice. *Development*, **149**(11): dev200516.

Zhang Y, Liu H, Li W, et al. 2017. Intraflagellar transporter protein (IFT27), an IFT25 binding partner, is essential for male fertility and spermiogenesis in mice. *Developmental Biology*, **432**(1): 125–139.

Zhang Y, Liu H, Li W, et al. 2018. Intraflagellar transporter protein 140 (IFT140), a component of IFT-a complex, is essential for male fertility and spermiogenesis in mice. *Cytoskeleton*, **75**(2): 70–84.

Zhang ZG, Li W, Zhang Y, et al. 2016. Intraflagellar transport protein IFT20 is essential for male fertility and spermiogenesis in mice. *Molecular Biology of the Cell*, **27**(23): 3705–3716.